

VLBI Observations of SiO Masers around AH Scorpii

Xi Chen¹ & Zhi-Qiang Shen¹

ABSTRACT

We report the first Very Long Baseline Array (VLBA) observations of 43 GHz $v=1$, $J=1-0$ SiO masers in the circumstellar envelope of the M-type semi-regular supergiant variable star AH Sco at 2 epochs separated by 12 days in March 2004. These high-resolution VLBA images reveal that the distribution of SiO masers is roughly on a persistent elliptical ring with the lengths of the major and minor axes of about 18.5 and 15.8 mas, respectively, along a position angle of 150° . And the red-shifted masers are found to be slightly closer to the central star than the blue-shifted masers. The line-of-sight velocity structure of the SiO masers shows that with respect to the systemic velocity of -6.8 km s^{-1} the higher velocity features are closer to the star, which can be well explained by the simple outflow or infall without rotation kinematics of SiO masers around AH Sco. Study of proper motions of 59 matched features between two epochs clearly indicates that the SiO maser shell around AH Sco was undergoing an overall contraction to the star at a velocity of $\approx 13 \text{ km s}^{-1}$ at a distance of 2.26 kpc to AH Sco. Our 3-dimensional maser kinematics model further suggests that such an inward motion is very likely due to the gravitation of the central star. The distance to AH Sco of $2.26 \pm 0.19 \text{ kpc}$ obtained from the 3-dimensional kinematics model fitting is consistent with its kinematic distance of 2.0 kpc.

Subject headings: circumstellar matter — masers — stars: individual (AH Sco)
— stars: kinematics

1. Introduction

AH Scorpii (AH Sco) is a semi-regular variable with an optical period of 714 days (Kukarkin et al. 1969) and a spectral type of M5Ia-Iab (Humphreys 1974). The systemic velocity of AH Sco is estimated to be about -7 and -3 km s^{-1} based on the observations of OH maser (Baudry, Le Squeren & Lépine 1977) and H₂O maser (Lépine, Pase de Barros

¹Shanghai Astronomical Observatory, 80 Nandan Road, Shanghai 200030, P.R.China

& Gammon 1976), respectively. The distance to AH Sco remains uncertain. A photometric distance of 4.6 kpc has been derived by Humphreys & Ney (1974) based on their infrared data. However, Baudry, Le Squeren & Lépine (1977) led to a photometric distance of 2.6 kpc under an assumption of an absolute visual magnitude of -5.8 for Iab stars, whereas its kinematic distance was about $1.5 \sim 2.0$ kpc for its systemic velocity $-5.5 \sim -7.5$ km s $^{-1}$.

Late type stars often exhibit circumstellar maser emission in molecules OH, H $_2$ O, and SiO. The supergiant variable AH Sco is such a star that has been detected strong maser emission with single-dish in all three species (e.g. Lépine, Pase de Barros & Gammon 1976; Baudry, Le Squeren & Lépine 1977; Balister et al. 1977, Gómez Balboa & Lépine 1986). The interferometric observations of these masers would be useful in determining the structure and kinematics of the circumstellar envelop (CSE) and understanding the physical circumstance and mass loss procedure for this supergiant variable. Unfortunately, there has been so far no any published interferometric map of OH, H $_2$ O and SiO masers toward this source.

Especially, SiO masers provide a good probe of the morphology of CSE and kinematics of gas in the extended atmosphere which is a complex region located between the photosphere and the inner dust formation shell. Previous VLBI experiments have demonstrated ringlike configurations (e.g. Diamond et al. 1994; Greenhill et al. 1995; Boboltz, Diamond & Kemball 1997; Yi et al. 2005, Chen et al. 2006), or elliptical distributions (e.g. Boboltz & Marvel 2000; Sánchez et al. 2002; Boboltz & Diamond 2005) of SiO masers, and also revealed complex kinematics in SiO maser regions, e.g. contraction and expansion at the different phase of stellar pulsation (Boboltz, Diamond & Kemball 1997; Diamond & Kemball 2003; Chen et al. 2006) and even rotation (Boboltz & Marvel 2000; Hollis et al. 2001; Sánchez et al. 2002; Cotton et al. 2004; Boboltz & Diamond 2005). The ringlike or elliptical distribution that is assumed to be centered at the stellar position with a radius of 2–4 R_* suggests that SiO masers are amplified in tangential rather than radial path.

In this paper, we present the first VLBI maps of SiO maser emission toward AH Sco observed at two epochs separated by 12 days in March 2004. The observations and data reduction are described in § 2; results and discussions are presented in § 3, followed by conclusions in § 4.

2. Observations and data reduction

The observations of the $v = 1$, $J=1-0$ SiO maser emission toward AH Sco ($\alpha = 17^h 11^m 16.98^s$, $\delta = -32^\circ 19' 31.2''$, J2000) were performed at two epochs on March 8, 2004 (hereafter epoch A) and March 20, 2004 (hereafter epoch B) using the 10 stations of the Very Long Baseline

Array (VLBA) of the NRAO¹. A reference frequency of 43.122027 GHz was adopted for the $v=1$, $J=1-0$ SiO transition. The data were recorded in left circular polarization in an 8 MHz band and correlated with the FX correlator in Socorro, New Mexico. The correlator output data had 256 spectral channels, corresponding to a velocity resolution of 0.22 km s⁻¹. The system temperatures and sensitivities were on the order of 150 K and 11 Jy K⁻¹, respectively, for both epochs.

For the data reduction, we followed the standard procedure for VLBA spectral line observations using the Astronomical Image Processing System (AIPS) package. The band-pass response was determined from scans on the continuum calibrator (NRAO530). The amplitude calibration was achieved using the total-power spectra of AH Sco based on the “template spectrum” method. The template spectra at each epoch were obtained from the Mauna Kea (MK) station at a high elevation. A zenith opacity of about 0.05 at MK station estimated from the variation of system temperature with zenith angle was applied to correct the atmosphere absorption for each epoch. Residual group delays determined from a fringe fitting to the continuum calibrator were applied to the spectral line data. Residual fringe-rates were obtained by performing a fringe-fitting on a reference channel (at $V_{\text{LSR}} = -9.4$ km s⁻¹), which has a relatively simple structure in the maser emission. An iterative self-calibration on the reference channel was performed to remove any structural phase. The solutions of fringe-fitting and self-calibration were then applied to the whole spectral line data. Image cubes were produced for all the velocity channels between 14 and -18 km s⁻¹ with a synthesized beam of $0.69 \text{ mas} \times 0.20 \text{ mas}$ at a position angle -6° . Off-source rms noise (σ_{rms}) in channel maps ranges from 20 mJy beam⁻¹ in the maps with weak or no maser emission to 50 mJy beam⁻¹ in the maps containing strong maser emission. The flux densities, and positions in right ascension (R.A.) and declination (Dec.) for all emission components with intensity above $8 \sigma_{\text{rms}}$ in each channel maps were determined by fitting a two-dimension Gaussian brightness distribution using the AIPS task SAD. Errors in R.A. and Dec. obtained from above fitting procedure range from 1 μas for components with high SNR, to 168 μas for components with low SNR, and the typical uncertainty of the fitted position of maser components was smaller than 10 μas .

The remaining analysis of the maser component identifications was performed outside of the AIPS package. As described in our previous work (Chen et al. 2006), a maser spot is a single velocity component of the maser emission in each velocity channel map; a maser feature is a group of the maser spots within a small region in both space and Doppler velocity, typically 1 AU and 1 km s⁻¹, and is expected to be a physical feature consisting of a single

¹The National Radio Astronomy Observatory is a facility of the National Science Foundation operated under cooperative agreement by Associated Universities, Inc.

gas clump. In order to study the characteristics of SiO masers, it is necessary to identify maser features for each epoch. The maser spots in different channels were deemed as the same feature according to the criterion that these spots appear in at least three adjacent channels and lie within an angular separation of 0.5 mas. Finally, 82 and 87 maser features were identified for epochs A and B, respectively.

3. Results and Discussions

3.1. The spatial structure of the SiO masers

The full lists of parameters for each identified feature are given in Tables 1 and 2, for epochs A and B, respectively. We fit a Gaussian curve to the velocity profile of a feature containing at least four spots to determine V_{LSR} at the peak of velocity profile. For some features which can not be well represented by a Gaussian profile (labelled by a “*” in Tables 1 and 2), intensity weighted mean V_{LSR} was adopted. The velocity range across the feature Δu , is defined to be the difference between the maximal and minimal velocities of the spots in the feature. Feature positions (x, y) in R.A. and Dec. were determined from an intensity weighted average over maser spots in the feature. The uncertainty (σ_x, σ_y) of a feature position was defined as squared root of the square sum of (1) the mean spot distance from the defined feature position and (2) the mean measurement error of the spot positions. The weights proportional to the intensity of the spot were applied in the uncertainty estimation. The typical position uncertainties of features are 0.01 mas and 0.02 mas for R.A. and Dec., respectively. The positions are measured with respect to the reference feature at (0, 0) for aligning the maps in the two epochs (labelled by “R” in Tables 1 and 2; see Sect. 3.2.2). The distance of a maser feature, r , is measured with respect to the fitted center obtained from the ellipse model fitting to the distribution of maser features (see below). The flux density of the brightest spot in each feature was deemed as its peak flux density, P .

In two top panels of Figure 1, we compare the total power imaged by the VLBA (open circle) to the total power (solid line) obtained from the MK antenna for each epoch. The total power imaged by VLBA is obtained by summing all fitted flux of spots belonging to features. The fractional power representing the ratio of the total flux imaged by VLBA to the total flux of maser emission is shown in two bottom panels. The fraction is mostly between 0.4 and 0.8. That is, on average about $\sim 60\%$ of the total luminosity of masers was detected in our observations. Actually, such a fractional power reflects the degree of extension of the maser emission. If the apparent sizes of maser components are larger than that of the interferometric beam, the maser would be partly resolved (i.e. the fractional power is less than 1) and the fractional power should decrease with the increase of apparent

size of masers. The typical size of maser spots estimated from geometric mean of sizes of the major and minor axes of the spots, which were obtained by fitting to an elliptical Gaussian brightness distribution in the CLEAN map, is 0.5 mas. This typical scale size is slightly larger than the geometric mean of the VLBA beam of 0.4 mas. Thus $\sim 40\%$ missing flux in our map is mainly due to the high spatial resolution of the interferometric array.

Figure 2 shows the distributions of maser features toward AH Sco for the two epochs. These high resolution VLBI images reveal a persistent elliptical structure of SiO masers around AH Sco during an interval of 12 days. We characterized this morphology by performing a least-squares fit of an ellipse to the distribution of masers weighted by the flux density of each feature for each of two epochs. The best-fitting ellipses and the ellipse centers are also shown in Figure 2. The lengths of the major and minor axes were found to be 18.6 and 15.7 mas for epoch A, and 18.4 and 15.9 mas for epoch B, respectively, with the major axis of the ellipse oriented similarly at $\sim 150^\circ$ at both epochs. And the fitted centers of the elliptical distributions are almost the same at both epochs of -7.9 and 5.8 mas in R.A. and Dec., respectively. At a distance to AH Sco of 2.26 kpc (see Sect. 3.2.3), the distribution of SiO masers corresponds to about 42×35 AU for both two epochs. However, an axial ratio of 1.18 suggests that the distribution of maser features around AH Sco can be viewed approximately as the ringlike structure with an average diameter of about 17.2 mas (obtained from the geometric average of the major and minor axes for both epochs).

The simultaneous near-infrared interferometry and radio interferometry imaging of circumstellar SiO maser for late type stars have been done recently (e.g. Boboltz & Wittkowski 2005; Wittkowski et al. 2007; Cotton et al. 2004, 2006). These observations reveal that the ratio of the maser ring radius to the photospheric radius of the central star is about 1.5 – 4.0. Unfortunately, there has been no any published photospheric radius measurement for AH Sco. Thus we can not directly compare SiO maser ring radius with stellar radius for AH Sco.

We also notice that the red-shifted SiO masers lie slightly closer to the center than the blue-shifted masers (see Figure 2). This can be seen more clearly in Figure 3, showing the maser feature distance from the fitted center versus its line-of-sight (LOS) velocity (see Sect. 3.2.1). This phenomenon seems to be explained under the assumption that maser gas was undergoing infall to the central star. This is because along the same LOS path the red- and blue-shifted masers would appear in front of and behind the star, respectively, as long as the coherence path lengths satisfy the requirement of maser excitation, under the condition that the maser gas was undergoing infall to the central star during our observations. However the blue-shifted masers generated behind star would be obscured by the stellar disc projected on the LOS, while the red-shifted masers would not. Thus only red-shifted maser emission will be seen closer to the center. Actually, we have confirmed that the SiO maser shell contracts

to the star during our observations in Sect. 3.2.2. Moreover, from Figure 3, some systemic masers with velocity -7 km s^{-1} (see Sect. 3.2.1) locate at the distance of 7 mas which can be viewed as an upper limit to the photospheric radius, then the extreme blue-shifted masers with the distance of less than 7 mas would be obscured. This is consistent with our data (see Figure 3) showing that all blue-shifted masers locate at the distance of larger than 7 mas.

3.2. The kinematics of the SiO masers

3.2.1. The kinematics obtained from LOS velocities

From Figure 2, we notice that there appears a velocity gradient at both epochs, with the bluest- and reddest-shifted maser features lying closer to the center of the distribution than those with intermediate velocities. To verify this, we plotted in Figure 3 feature distance from the fitted center (marked by the red star in Figure 2) versus its LOS velocity for both epochs. Both epochs appear to have the same distribution with a peak near the velocity of -7 km s^{-1} and decreasing maser distance with increasing deviation of velocity from this peak velocity. This has also been seen in some OH maser sources (e.g. Reid et al. 1977, Chapman & Cohen 1986), H_2O maser sources (e.g. Yates & Cohen 1994) and SiO maser sources (e.g. Boboltz & Marvel 2000; Wittkowski et al. 2007). A widely used simple model to explain this phenomenon is that of a uniformly expanding thin shell (e.g. Reid et al. 1977; Yates & Cohen 1994; Wittkowski et al. 2007). In this model the projected distance r (in the fourth column of Tables 1 and 2) of a maser on the shell from the center is related to its LOS velocity V_{LSR} by the expression

$$\left(\frac{r}{r_s}\right)^2 + \left(\frac{V_{\text{LSR}} - V_*}{V_{\text{exp}}}\right)^2 = 1, \quad (1)$$

where V_* is the systemic velocity of maser source, r_s is the shell radius and V_{exp} is the expanding velocity. Apparently, this model traces an ellipse on the $r - V_{\text{LSR}}$ plot.

The uniformly expanding thin shell model was used to characterize the expansion or contraction kinematics of a circular maser distribution. For the case of AH Sco, even though we characterize the maser distribution as an ellipse, an axial ratio of ~ 1.2 suggests that the distribution of maser features is approximately a circular structure as discussed in Section 3.1. Thus, we can also apply the uniformly expanding thin shell model to AH Sco. Moreover, most maser features locate in the northwest and southeast (i.e. the direction of major axis), and only few maser features locate in the northeast and southwest (i.e. the direction of minor

axis). These make the assumption of uniformly expansion/contraction in all directions of the uniformly expanding thin shell model to be suitable for the case of AH Sco. We performed a least-squares fit of the uniformly expanding thin shell model to the distribution of epochs A and B. The LSR stellar velocity of AH Sco, which is estimated to be about -7 and -3 km s^{-1} based on the observations of OH maser (Baudry, Le Squeren & Lépine 1977) and H_2O maser (Lépine, Pase de Barros & Gammon 1976), has not been measured particularly well yet. Thus the LSR stellar velocity V_* , together with the shell radius r and expansion velocity V_{exp} , is treated as a free parameter in the fitting procedure. The values of V_* , V_{exp} and r_s were found to be -6.8 ± 0.5 km s^{-1} , 18.8 ± 2.0 km s^{-1} and 9.3 ± 0.1 mas, respectively, for both epochs, where the uncertainties are their standard errors. The best fitted $r - V_{\text{LSR}}$ ellipse is also plotted in Figure 3. The systemic velocity of AH Sco of -6.8 km s^{-1} is consistent with the value of -7 km s^{-1} from the OH maser observations. The shell radius of 9.3 mas determined from above model fitting is larger than the radius of maser distribution of 8.6 mas (see Sect. 3.1). A note is that the definition of the shell radius determined from the uniformly expanding thin shell model is different from that of the radius of the maser distribution. The shell radius reflects the scale of a 3-dimensional maser spherical shell, whereas the radius of maser distribution reflects the scale of maser distribution in the sky plane, and is the projected size on the sky plane of the 3-dimensional spherical shell. Thus it is not surprising that the shell radius is a bit larger than the radius of maser distribution.

For comparison, the escape velocity calculated at the shell radius of 9.3 mas, assuming a typical mass of $10 M_\odot$ for supergiant and a distance to AH Sco of 2.26 kpc, is about 29 km s^{-1} . Thus, the expansion/contraction velocity at the location of SiO maser shell is less than the corresponding escape velocity, suggesting that the maser gas is still gravitational bound to the star. However, the current fitting can not tell the sign of V_{exp} term (as can be seen in Eq. (1)), and thus can not differentiate between expansion and contraction of the maser shell. The dominant expansion or contraction of maser shell can be clarified by the SiO maser proper motion analysis to be discussed below.

3.2.2. Maser Proper Motions

We can study proper motion and the kinematics of the CSE of AH Sco by tracing the matched features that appeared in both epochs. Because the absolute position of the phase center in each image is not kept during the data reduction, we must align two-epoch maps for studying the proper motion. The feature used for registration is the one with a velocity $V_{\text{LSR}} \approx -9.3$ km s^{-1} (labelled by “R” in Tables 1 and 2) at both epochs. And then we shift the coordinate frames for both epochs to align the origin $(0, 0)$ with this feature. At an

assumed distance of 2.6 kpc (Baudry et al. 1977) and a maximum expansion/contraction velocity of 20 km s^{-1} (see Sect. 3.2.1), the maser proper motion should be less than 0.05 mas in an interval of 12 days. Thus we can match these features from one epoch to another epoch using the criterion that the angular separation of the matched features between two epochs should not exceed 0.15 mas after allowing the maximum position uncertainty of (0.05, 0.10) mas (see Tables 1 and 2) and they have similar velocity profile and flux density. As a result, we identified 59 commonly matched maser features between two epochs (see Tables 1 and 2). Actually, using a reference feature located on the maser shell to align maps for two epochs could introduce a constant offset vector representing the motion of the reference feature in the individual maser proper motions. We assumed that the vector-average of the proper motions for all the matched features represents the motion of the aligned feature. In order to present a better representation of the real motions of individual features, the mean proper motion was subtracted from each of the determined proper motion vectors. The proper motions of matched maser features are shown in Figure 4. Here we adopt the distance to AH Sco of 2.26 kpc (see Sect. 3.2.3) for denoting the velocity values of the proper motions.

From Figure 4, we can clearly see that the maser shell shows an overall contraction toward the central star. In order to better characterize the net contraction of the masers, we computed the separations between pairwise combinations of features. This technique has previously been applied to analyse proper motions of OH masers (Chapman, Cohen & Saika 1991; Bloemhof, Reid & Moran 1992), H_2O masers (Boboltz & Marvel 2007), and SiO masers (Boboltz, Diamond & Kemball 1997; Chen et al. 2006), and has no dependence on the alignment of maps. The procedure involves computing the angular separation between two features at the first epoch and the separation between the corresponding two features at the second epoch. The difference between the two values of separation is referred to as the pairwise separation. The procedure is repeated for all the possible pair combinations. However, the inclusion of all possible pair combinations often results in decreasing toward zero due to the bias caused by calculating pairs of closely spaced maser features. For the sake of clarity, and to determine representative values for the angular shifts due to the contraction, we have included only those pairs separated by more than 9 mas (corresponding to the radius of maser distribution). We obtained the mean value of these pairwise separations of -0.039 ± 0.002 mas, in an interval of 12 days, corresponding to a proper motion of $-1.186 \pm 0.061 \text{ mas yr}^{-1}$ or a velocity of $-12.7 \pm 0.7 \text{ km s}^{-1}$ at a distance of 2.26 kpc, where the uncertainties are the standard errors. The negative value of proper motion implies an overall contraction of the maser shell. The contraction value of $1.186 \pm 0.061 \text{ mas yr}^{-1}$ of maser shell derived from the pairwise separation is significantly less than the scalar-averaged value of SiO proper motions of $1.96 \pm 0.15 \text{ mas yr}^{-1}$ (where its uncertainty is the standard

error). This is because some of maser proper motions do not completely point to the center or even a few proper motions show outflow motion as can be seen in Figure 4.

The contraction of SiO maser shell has been reported in two Mira variables R Aqr (Boboltz, Diamond & Kemball 1997) and TX Cam (Diamond & Kemball 2003) and one red supergiant VX Sgr (Chen et al. 2006; 2007). Our observations provide an inward motion of SiO maser shell around another red supergiant AH Sco. In Table 3 we list these four sources. We also estimated the stellar optical phase of AH Sco at our observation sessions to be $\phi \simeq 0.55$ (i.e. at the optical minimum phase) based on the American Association of Variable Star Observers (AAVSO) data. Interestingly, the optical phase at which the SiO maser shell around the red supergiant AH Sco contracts is nearly the same as that seen in other three sources: VX Sgr ($\phi = 0.75 - 0.80$; Chen et al. 2006), R Aqr ($\phi = 0.78 - 0.04$; Boboltz, Diamond & Kemball 1997), TX Cam ($\phi = 0.50 - 0.65$; Diamond & Kemball 2003). This infers that the contraction of the SiO maser shell would occur during an optical stellar phase of $0.5 - 1$, which agrees with the previous conclusion reported by Chen et al. (2006) and the theoretical kinematical model results of Humphreys et al. (2002). Moreover, from Table 3 we can find that the contraction velocity of about 13 km s^{-1} of maser shell around AH Sco is the largest among the four sources.

3.2.3. 3-dimensional kinematics model for SiO masers

In order to estimate further the kinematical parameters of SiO masers and the distance to AH Sco, we made model-fitting to analyze spatial distribution and proper motion of SiO maser features as done by Gwinn, Moran & Reid (1992) and Imai et al. (2000; 2003). The model fitting requires to minimize the squared sum of the differences between the observed and model velocities,

$$\chi^2 = \sum_i \left\{ \frac{[\mu_{ix} - V_{ix}/(a_0d)]^2}{\sigma_{ix}^2} + \frac{[\mu_{iy} - V_{iy}/(a_0d)]^2}{\sigma_{iy}^2} + \frac{[u_{iz} - V_{iz}]^2}{\sigma_{iz}^2} \right\}, \quad (2)$$

where, μ_{ix} and μ_{iy} are the observed proper motions in R.A. and Dec., respectively, and u_{iz} the observed velocity along LOS, d the distance to the maser source, $a_0 \equiv 4.74 \text{ km s}^{-1} \text{ mas}^{-1} \text{ yr kpc}^{-1}$, $(\sigma_{ix}, \sigma_{iy}, \sigma_{iz})$ the standard deviations of the observed velocity vectors which are determined in the similar manner of Imai et al. (2002). In this work, we assume a spherically expanding flow in SiO maser region, thus the model velocity vector \mathbf{V}_i (including V_{ix} , V_{iy} in R.A. and Dec., and V_{iz} in LOS) for the i th maser feature can be expressed as

$$\mathbf{V}_i = \mathbf{V}_0 + V_{exp}(i) \frac{\mathbf{r}_i}{r_i}, \quad (3)$$

$$\mathbf{r}_i = \mathbf{x}_i - \mathbf{x}_0 \text{ (or } r_{ix} = x_i - x_0, r_{iy} = y_i - y_0, r_{iz} = z_i), \quad (4)$$

where \mathbf{V}_0 (v_{0x}, v_{0y}, v_{0z}) is a systemic velocity vector of the stellar system, reflecting the motion of the central star; $V_{exp}(i)$ is an expanding velocity as a function of the distance from the origin of the flow, r_i ; \mathbf{x}_0 ($x_0, y_0, 0$) is the position vector of the flow origin with respect to the position of reference maser feature (here, we assumed that the origin of the flow was at the star, whose positions of $x_0 = -7.94$ mas and $y_0 = -5.83$ mas have been derived from the least-squares fit of an ellipse to the distribution of masers in Sect. 3.1.); and (x_i, y_i) is an observed position of maser feature on the sky plane; the position of a maser feature along the LOS, z_i is estimated as one of the free parameters too (Imai et al. 2000). In the model fitting procedure, we adopted the expanding velocity as $V_{exp}(i) = V_1(r_i/r_0)^\alpha$, where V_1 is the expansion velocity at a unit distance of $r_0 \equiv 10$ mas, and α a power-law index indicating the apparent acceleration or deceleration of the flow. Moreover, we excluded those maser features with large positive expansion velocities in the fitting. Finally, we used 48 proper motion data and obtained the best solutions with their standard errors, which are given in Table 4.

From Table 4, we can see that a negative expansion velocity of -14.1 ± 1.4 km s⁻¹ at a shell radius of 10 mas was estimated from the best-fit model, supporting the presence of a real contracting flow in the SiO maser region around AH Sco. This is consistent with the conclusion derived from the pairwise separation calculation in Sect. 3.2.2. For comparison, we also estimate the corresponding velocity of -15.0 ± 1.5 km s⁻¹ at the mean SiO maser radius of 9 mas according to the power-law index of the acceleration of the flow α obtained in our model. However, the velocity of -15.0 ± 1.5 km s⁻¹ seems larger than that of -12.7 ± 0.7 km s⁻¹ obtained from the pairwise separation analysis, which is because that we excluded maser features showing outflow motion in the 3-dimensional kinematics model fitting procedure. And the velocity of 15.0 ± 1.5 km s⁻¹ is slightly smaller than that of 18.8 ± 2.0 km s⁻¹ obtained from a least-squares fit of the uniformly expanding thin shell model to SiO maser LOS velocity structure (see Sect. 3.2.1), which is due to that some maser proper motions used in model fitting still deviate from the originating point of the inflow (i.e. the position of central star; see Figure 4), whereas the model fitting method involves one critical assumption that velocity vectors are in the radial direction from the commonly originating point of the flow. The systemic velocity along LOS of $v_{0z} = -5.2$ km s⁻¹ from the 3-dimensional kinematics model is also roughly consistent with that of -6.8 km s⁻¹ derived from the uniformly expanding thin shell model in Sect. 3.2.1, suggesting that the assumption of the origin of the flow located at the star is reasonable. More interestingly, we obtain a negative power-law index of the acceleration of the flow, $\alpha = -0.54 \pm 0.16$, indicating that the contracting flow was accelerating in the SiO maser region with a similar

form of $v \sim r^{-0.5}$ of the gravitational contraction. Thus the 3-dimensional maser kinematics model suggests that the infall motions of SiO masers can be achieved under the gravitational effect of the central star.

The velocity gradient across the SiO maser region usually used in the numerical simulation of SiO masers (e.g. Doel et al. 1995; Humphreys et al. 2002) can be expressed by

$$\varepsilon = \frac{d \ln V}{d \ln r} = \frac{r dV}{V dr}. \quad (5)$$

A value of $\varepsilon = 0$ corresponds to a constant velocity expansion, while $\varepsilon \geq 1$ corresponds to a velocity field with large radial accelerations. A value of $\varepsilon = 1$ was usually adopted in the SiO maser numerical simulations (e.g. Doel et al. 1995). Chapman & Cohen (1986) estimated the velocity gradient ε for the OH, H₂O and SiO maser emission around VX Sgr and found that $\varepsilon \approx 0.2$ in the 1612 MHz OH maser region, $\varepsilon \approx 0.5$ in the region of the H₂O and mainline OH masers, and $\varepsilon \approx 1$ in SiO maser region. However, the power-law index of the acceleration of the flow ($\alpha = -0.54 \pm 0.16$) derived from our best-fit kinematic model suggests a negative velocity gradient value of $\varepsilon = -0.54$ in SiO maser region around AH Sco. This is different from those flows that apparently exhibit the accelerations in their SiO maser kinematics (e.g. VX Sgr, Chapman & Cohen 1986; S Ori, Wittkowski et al. 2007) and the positive velocity gradient value used in the maser simulations. The content of maser simulations is beyond this work. However, we think that such a negative velocity gradient ε adopted in maser simulation may be necessary for understanding the SiO maser emission, especially during the infall stage of the SiO maser shell.

The 3-dimensional kinematics model fitting shows a best solution for the distance to AH Sco of 2.26 ± 0.19 kpc. This distance value seems reasonable. Firstly, this distance of AH Sco is in a good agreement with its estimated ‘near’ kinematic distance of about 2.0 kpc at the systemic velocity of -6.8 km s⁻¹ with the adopted galactic constants, $R_{\odot} = 8.5$ kpc and $\Theta_{\odot} = 220$ km s⁻¹. Secondly, at the distance of 2.26 kpc, the scalar-averaged value of 1.96 ± 0.15 mas yr⁻¹ of proper motions of matched features (shown in Figure 4) would correspond to a velocity of 21.0 ± 1.6 km s⁻¹. This velocity is consistent with the expansion/contraction velocity of 18.8 ± 2.0 km s⁻¹ in SiO maser region obtained from a least-squares fit of the uniformly expanding thin shell model to LOS velocity structure. Thus we adopt the distance to AH Sco of 2.26 kpc throughout this work.

4. Conclusions

We summarize the main results obtained from 2-epoch (at an interval of 12 days) monitoring observations of the 43 GHz $v = 1, J = 1 - 0$ SiO maser emission toward AH Sco performed in March 2004, corresponding to a stellar optical phase of ~ 0.55 .

- (1). Our observations revealed a persistent elliptical structure of SiO masers with the sizes of the major and minor axes of about 18.5 and 15.8 mas, respectively, along a position angle of 150° . We notice that the red-shifted SiO maser emission lies slightly closer to the center than the blue-shifted one.
- (2). The LOS velocity structure of the SiO masers shows a velocity gradient at both epochs, with masers toward the blue- and red-shifted ends of the spectrum lying closer to the center of the maser distribution than masers at intermediate velocities, which can be explained by the outflow or infall kinematics of SiO maser shell. By analyzing the uniformly expanding thin shell model to the LOS velocity of SiO masers, we estimated the expansion/contraction velocity of about 19 km s^{-1} in SiO maser region around AH Sco.
- (3). The proper motions of 59 matched features between two epochs show that the SiO maser shell around AH Sco was undergoing inward motion to the central star. Computing pairwise separation of these matched features, we obtained that the maser shell contracts toward AH Sco with a velocity of about 13 km s^{-1} at a distance to AH Sco of 2.26 kpc. The stellar optical phase of red supergiant AH Sco is very close to that of Mira variables R Aqr and TX Cam and red supergiant VX Sgr when the SiO maser shell contracts. And the contraction velocity of about 13 km s^{-1} of maser shell around AH Sco is the largest one among the known four sources showing contraction of SiO maser shell.
- (4). We made a 3-dimensional kinematics model to analyze spatial distribution and proper motion of SiO maser features. The 3-dimensional maser kinematics model further suggested that the contraction of SiO maser shell around AH Sco is mainly due to the gravitation of the central star. And the distance to AH Sco of $2.26 \pm 0.19 \text{ kpc}$ estimated from this kinematics model fitting is consistent with the kinematic distance of 2.0 kpc at the systemic velocity of AH Sco of -7 km s^{-1} .

We thank an anonymous referee for helpful comments that improved the manuscript. We also acknowledge with thanks data from the AAVSO International Database based on observations submitted to the AAVSO by variable star observers worldwide.

This work was supported in part by the National Natural Science Foundation of China (grants 10573029, 10625314, and 10633010) and the Knowledge Innovation Program of the Chinese Academy of Sciences (Grant No. KJCX2-YW-T03), and sponsored by the Program of Shanghai Subject Chief Scientist (06XD14024) and the National Key Basic Research Development Program of China (No. 2007CB815405).

X. Chen thanks the support by the Knowledge Innovation Program of the Chinese Academy of Sciences. ZQS acknowledges the support by the One-Hundred-Talent Program of Chinese Academy of Sciences.

REFERENCES

- Balister, M., Batchelor, R. A., Haynes, R. F., Knowles, S. H., Mc Culloch, M. G., Robinson, B. J., Wellington, K. J., & Yabsley, D. E. 1977, *MNRAS*, 180, 415
- Baudry, A., Le Squeren, A. M., & Lépine, J. R. D. 1977, *A&A*. 54,593
- Bloemhof, E. E., Reid, M. J., & Moran, J. M. 1992, *ApJ*, 397, 500
- Boboltz, D. A., Diamond, P. J., & Kemball, A. J. 1997, *ApJ*, 487, L147
- Boboltz, D. A., & Diamond, P. J. 2005, *ApJ*, 625, 978
- Boboltz, D. A., & Marvel, K. B., 2007, *ApJ*, 665, 680
- Boboltz, D. A., & Marvel, K. B. 2000, *ApJ*, 545, L149
- Boboltz, D. A., & Wittkowski, M. 2005, *ApJ*, 618, 953
- Chapman, J. M., & Cohen, R. J. 1986, *MNRAS*, 220, 513
- Chapman, J. M., Cohen, R. J., & Saika, D. J. 1991, *MNRAS*, 249, 227
- Chen, X., Shen, Z.-Q., Imai, H., & Kamohara, R. 2006, *ApJ*, 640, 982
- Chen, X., Shen, Z.-Q., & Xu, Y. 2007, *ChJA&A*, 7, 531
- Cotton, W. D., et al. 2006, *A&A* 456, 339
- Cotton, W. D., et al. 2004, *A&A*, 414, 275
- Diamond, P. J., Kemball, A. J., Junor, W., Zensus, A. Benson, J., & Dhawan, V. 1994, *ApJ*, 430, L61

- Diamond, P. J., & Kembball, A. J. 2003, *ApJ*, 599, 1372
- Doel, R. C., Gray, M. D., Humphreys, E. M. L., Braithwaite, M. F., & Field, D. 1995, *A&A*, 302, 797
- Gómez Balboa, A. M., & Lepine, J. R. D. 1986, *A&A*, 159, 166
- Greenhill, L. J., Colomer, F., Moran, J. M., Danchi, W. C., & Bester, M. 1995, *ApJ*, 449, 365
- Gwinn, C. R., Moran, J. M., & Reid, M. J. 1992, *ApJ*, 393, 149
- Hollis, J. M., Boboltz, D. A., Pedelty, J. A., White, S. M., & Forster, J. R. 2001, *ApJ*, 559, L37
- Humphreys, R. M. 1974, *ApJ*, 188, 75
- Humphreys, E. M. L., & Gray, M. D., Yates, J. A., Field, D., Bowen, G. H., & Diamond, P. J. 2002, *A&A*, 386, 256
- Humphreys, R. M., Ney, E. P. 1974, *ApJ*, 194, 623
- Imai, H., Kameya, O., Sasao, T., Miyoshi, M., Deguchi, S., Horiuchi, S., & Asaki, Y. 2000, *ApJ*, 538, 751
- Imai, H., et al. 2003, *ApJ*, 590, 460
- Kukarkin, B. V., et al. 1969. *General Catalogue of Variable Stars*, 3rd edn., Astronomical Council of the Academy of Sciences in the USSR, Moscow.
- Lépine, J. R. D., Pase de Barros, M. H., & Gammon, R. H. 1976, *A&A*, 48, 269
- Reid, M. J., Muhleman, D. O., Moran, J. M., Johnston, K. J., & Schwartz, P. R. 1977, *ApJ*, 214, 60
- Sánchez Contreras, C., Desmurs, J. F., Bujarrabal, V., Alcolea, J., & Colomer, F. 2002, *A&A*, 385, L1
- Wittkowski, M., Boboltz, D. A., Ohnaka, K., Driebe, T., & Scholz, M. 2007, *A&A*, 470, 191
- Yates, J. A., & Cohen, R. J. 1994, *MNRAS*, 270, 958
- Yi, J., Booth, R. S., Conway, J. E., & Diamond, P. J. 2005, *A&A*, 432, 531

Table 1. 43 GHz SiO maser features around AH Sco observed by VLBA on March 8, 2004.

ID	V_{LSR} (km s^{-1})	Δu	r (mas)	x (mas)	σ_x	y (mas)	σ_y	P (Jy)	S (Jy km s^{-1})	Match ID Epoch 2
(1)	(2)	(3)	(4)	(5)	(6)	(7)	(8)	(9)	(10)	(11)
1	-17.28	1.52	8.10	-2.862	0.002	-0.452	0.005	11.7	36.8	1
2*	-16.32	0.65	6.96	-1.356	0.009	7.974	0.032	0.7	2.1	...
3	-15.16	3.26	8.31	-1.637	0.004	0.448	0.008	19.7	147.5	2
4*	-14.94	0.87	8.76	-1.679	0.007	-0.250	0.022	1.5	4.9	...
5	-14.54	2.82	8.42	-1.304	0.003	0.686	0.008	16.6	84.3	6
6*	-14.16	0.87	8.56	-1.724	0.004	-0.018	0.015	8.2	21.0	...
7	-13.23	0.87	8.34	-3.051	0.004	-0.909	0.009	3.1	8.1	8
8	-12.56	1.09	8.45	-1.228	0.007	0.738	0.007	10.3	28.7	11
9	-12.22	3.04	8.87	-0.792	0.003	0.621	0.005	25.5	151.3	9
10	-11.98	2.17	8.38	-1.790	0.002	0.176	0.007	9.4	52.9	...
11	-10.94	2.17	9.47	-0.330	0.011	0.243	0.015	9.8	59.9	13
12	-9.97	1.30	9.04	-1.329	0.008	-0.305	0.019	4.5	18.9	14
13	-9.77	2.82	9.30	-0.957	0.003	-0.280	0.008	15.9	103.8	16
14	-9.57	1.09	8.39	-16.011	0.007	8.277	0.013	5.2	21.6	...
15 ^R	-9.31	2.39	9.88	0.000	0.005	0.000	0.007	35.9	254.8	18
16	-9.20	1.09	9.58	0.030	0.019	0.567	0.012	1.9	6.6	19
17*	-9.05	1.09	8.95	-15.261	0.009	11.052	0.036	3.5	10.1	20
18*	-9.04	0.87	8.93	-15.099	0.034	11.227	0.021	5.1	12.7	...
19	-8.96	1.95	9.39	-15.667	0.006	11.237	0.018	6.2	29.5	21
20	-8.68	1.74	10.21	0.412	0.008	0.014	0.026	6.7	23.3	22
21	-8.58	1.09	11.93	-16.001	0.009	14.662	0.029	1.4	6.0	23
22	-8.33	2.82	8.37	-15.791	0.009	8.848	0.016	5.3	40.4	27
23*	-8.32	0.65	11.59	-1.897	0.012	-4.038	0.028	1.2	3.1	...
24	-8.23	1.52	9.79	-12.858	0.006	14.322	0.019	4.4	19.2	25
25	-8.12	1.09	8.58	-14.846	0.005	10.985	0.014	7.5	26.2	24
26	-8.02	2.82	9.74	0.438	0.009	0.925	0.018	7.2	45.9	26
27	-7.80	1.74	7.91	-9.327	0.007	13.627	0.013	5.3	29.1	29
28	-7.56	1.09	11.10	-15.678	0.024	13.829	0.041	1.5	6.3	...
29	-7.55	1.09	7.13	-7.390	0.009	12.937	0.029	1.9	6.9	...
30	-7.07	1.74	11.44	-15.386	0.006	14.560	0.015	4.3	22.1	30
31	-6.72	1.09	8.24	-9.195	0.010	13.984	0.025	2.3	8.6	31
32	-6.70	2.39	6.90	-5.873	0.003	12.406	0.014	8.8	53.1	...
33	-6.45	1.74	9.34	-12.505	0.012	14.010	0.018	2.8	14.8	...
34*	-6.14	0.65	7.81	-7.069	0.011	13.593	0.032	1.2	2.8	...
35*	-6.10	0.65	9.38	-16.537	0.015	9.687	0.032	1.8	4.9	32
36	-5.53	1.52	8.82	-8.159	0.005	14.657	0.003	22.6	92.2	34
37	-4.58	1.74	9.07	-16.715	0.003	8.303	0.006	10.3	48.5	36
38	-4.20	1.09	8.88	-7.921	0.006	14.718	0.003	8.6	41.4	37
39*	-3.70	0.65	9.51	-17.329	0.024	4.082	0.039	2.4	6.4	39
40	-3.10	2.39	8.75	-16.673	0.007	4.814	0.016	11.2	67.2	43
41	-3.03	1.96	9.13	-7.780	0.006	14.967	0.008	12.4	75.7	41
42	-2.88	2.17	9.25	-16.938	0.008	8.141	0.009	6.7	44.6	42
43	-2.82	1.74	8.39	-16.237	0.013	4.292	0.024	3.5	13.5	47
44	-2.78	1.52	11.08	-14.008	0.016	15.137	0.026	2.2	10.0	46
45	-2.32	2.39	9.17	-16.406	0.006	9.461	0.009	12.9	79.8	45
46	-1.72	2.17	8.03	-15.938	0.009	4.691	0.018	7.2	46.0	48
47*	-1.50	0.87	8.27	-16.227	0.022	5.114	0.047	4.6	6.4	50
48*	-0.92	0.65	7.73	-15.366	0.015	3.546	0.043	2.0	5.5	...
49	-0.73	1.52	8.66	-15.946	0.017	9.235	0.038	3.8	15.5	...
50	-0.64	1.52	9.15	-11.534	0.012	-2.610	0.022	4.2	18.8	52
51	-0.57	1.09	9.96	1.832	0.021	7.554	0.029	1.6	7.2	53
52	0.25	1.09	7.10	-14.770	0.015	3.747	0.032	2.1	7.6	54
53	1.08	2.17	8.67	-11.042	0.014	-2.283	0.025	5.4	30.3	57
54*	1.30	0.65	8.07	-11.478	0.047	13.113	0.047	4.8	8.2	...
55	1.43	1.30	10.73	2.032	0.010	1.950	0.014	3.5	14.1	56
56	1.44	1.09	8.50	-10.621	0.005	-2.252	0.016	3.5	10.1	55
57*	1.48	0.65	8.23	-11.841	0.012	13.107	0.050	1.8	4.3	58
58	2.34	1.52	7.57	-11.300	0.005	12.637	0.021	8.4	36.4	61
59	2.65	1.95	8.11	-12.171	0.009	12.774	0.030	3.1	20.3	...
60	2.87	1.74	7.72	-2.150	0.014	0.760	0.021	1.8	11.9	65
61	3.19	1.09	7.08	-11.118	0.018	12.181	0.023	7.4	24.4	64
62	3.77	1.52	6.84	-10.486	0.006	12.202	0.016	4.0	16.7	66
63	3.86	1.52	7.73	-12.410	0.021	12.175	0.024	3.1	17.1	...
64*	3.86	0.65	7.38	-10.185	0.010	-1.221	0.045	1.6	4.0	68
65	4.04	1.30	7.43	-1.074	0.007	3.081	0.023	1.2	6.0	...

Table 1—Continued

ID	V_{LSR} (km s^{-1})	Δu (3)	r (mas)	x (mas)	σ_x (6)	y (mas)	σ_y (8)	P (Jy)	S (Jy km s^{-1})	Match ID Epoch 2 (11)
(1)	(2)	(3)	(4)	(5)	(6)	(7)	(8)	(9)	(10)	(11)
66	4.10	3.04	8.66	0.508	0.008	4.077	0.013	2.8	29.4	70
67	4.70	1.52	7.40	-12.565	0.009	11.650	0.020	5.8	30.0	71
68	4.83	1.30	6.67	-9.377	0.012	-0.696	0.033	2.3	10.2	...
69	5.20	1.95	7.22	-3.566	0.014	0.108	0.027	2.4	14.6	...
70	5.43	1.30	6.05	-10.355	0.003	11.399	0.012	5.5	19.7	75
71*	5.59	0.65	6.82	-4.651	0.008	-0.124	0.023	1.2	3.2	76
72	5.97	1.52	5.75	-13.283	0.009	3.593	0.016	2.5	15.5	74
73	7.00	1.30	6.21	-7.430	0.011	12.023	0.025	1.9	8.1	79
74	7.33	3.04	6.39	-9.017	0.006	-0.477	0.013	4.0	41.0	78
75	7.42	1.74	6.51	-8.278	0.008	12.338	0.022	2.9	16.6	...
76	7.73	2.17	5.08	-12.707	0.005	3.946	0.008	4.0	27.5	82
77*	7.99	0.65	7.79	-0.359	0.017	4.208	0.034	1.3	3.5	...
78*	8.01	1.09	6.16	-8.120	0.008	11.995	0.023	2.3	7.8	83
79*	8.35	1.09	3.98	-4.070	0.014	6.607	0.026	1.5	6.5	...
80	8.92	1.95	5.85	-8.965	0.006	0.059	0.023	4.9	31.9	84
81	9.17	1.30	5.85	-8.289	0.007	11.678	0.013	3.9	17.9	85
82	12.62	0.87	2.50	-5.479	0.009	5.706	0.017	2.2	7.4	86

Note. — column (1): ID number; columns (2): V_{LSR} at the peak of velocity profile of feature; column (3): the velocity range across the feature Δu ; column (4): distance of maser feature, r , from the fitted position of central star; columns (5) and (7): the intensity weighted centroid of each feature (x, y); columns (6) and (8): the corresponding uncertainties (σ_x, σ_y); column (9): the peak flux density of each feature P ; column (10): the integrated flux density of all spots in the feature S ; and column (11): the ID numbers of matched features at another epoch.

*Feature which can not be well represented by a Gaussian curve.

^RReference feature.

Table 2. 43 GHz SiO maser features around AH Sco observed by VLBA on March 20, 2004.

ID	V_{LSR} (km s ⁻¹)	Δu	r (mas)	x (mas)	σ_x	y (mas)	σ_y	P (Jy)	S (Jy km s ⁻¹)	Match ID Epoch 2
(1)	(2)	(3)	(4)	(5)	(6)	(7)	(8)	(9)	(10)	(11)
1	-17.23	1.09	8.14	-2.861	0.003	-0.509	0.014	5.8	16.0	1
2	-15.14	2.39	8.33	-1.650	0.004	0.385	0.009	14.1	90.0	3
3*	-14.73	0.87	7.97	-1.642	0.012	0.953	0.021	2.5	3.8	...
4*	-14.60	0.87	8.03	-1.351	0.018	1.243	0.011	1.3	3.4	...
5*	-14.59	0.65	8.90	-1.271	0.010	-0.055	0.011	1.2	3.1	...
6	-14.50	2.39	8.39	-1.351	0.003	0.642	0.009	21.7	121.4	5
7*	-13.74	0.65	9.04	-0.905	0.052	0.159	0.091	2.1	5.5	...
8*	-13.31	0.65	8.37	-3.046	0.005	-0.946	0.017	2.0	4.4	7
9	-12.41	4.13	8.85	-0.813	0.006	0.591	0.015	18.9	144.1	9
10	-12.17	2.82	8.44	-1.777	0.004	0.080	0.016	6.6	42.7	...
11	-12.14	1.52	8.56	-1.139	0.016	0.640	0.012	15.4	61.6	8
12	-11.07	0.87	9.09	-0.930	0.010	0.054	0.018	7.9	24.6	...
13	-10.89	1.74	9.33	-0.423	0.021	0.318	0.014	11.1	53.6	11
14	-10.08	1.52	8.99	-1.366	0.006	-0.296	0.022	5.8	20.6	12
15*	-9.88	0.87	9.80	-0.906	0.017	-0.988	0.021	1.4	3.6	...
16	-9.72	3.48	9.27	-1.002	0.005	-0.301	0.010	14.7	109.9	13
17	-9.50	1.30	8.36	-15.994	0.010	8.099	0.029	3.6	18.3	...
18 ^R	-9.36	3.04	9.86	0.000	0.005	0.000	0.008	32.0	218.4	15
19	-9.16	1.52	9.54	-0.015	0.007	0.519	0.017	1.9	7.4	16
20	-8.98	1.30	8.97	-15.241	0.007	11.070	0.021	5.5	21.6	17
21	-8.83	2.61	9.35	-15.673	0.007	11.118	0.029	7.5	38.1	19
22*	-8.55	0.65	10.21	0.354	0.006	-0.109	0.026	5.9	11.4	20
23	-8.11	1.09	11.85	-16.001	0.006	14.542	0.021	2.6	11.5	21
24	-8.09	1.52	8.60	-14.867	0.006	10.958	0.016	8.8	36.0	25
25	-8.08	1.52	9.75	-12.873	0.009	14.265	0.026	3.1	15.2	24
26	-8.07	1.96	9.72	0.428	0.012	0.887	0.027	6.7	37.0	26
27	-8.00	2.17	8.39	-15.780	0.009	8.829	0.017	9.6	49.4	22
28	-7.75	1.96	6.78	-5.908	0.005	12.333	0.017	4.2	22.0	...
29	-7.41	2.17	7.81	-9.290	0.009	13.558	0.024	3.8	21.6	27
30	-7.09	1.30	11.35	-15.398	0.011	14.414	0.031	3.2	17.1	30
31*	-6.99	1.30	8.21	-9.175	0.012	13.978	0.033	3.2	7.1	31
32	-6.34	1.52	9.39	-16.524	0.017	9.659	0.045	2.2	11.9	35
33	-6.31	1.52	9.17	-12.445	0.012	13.846	0.027	2.4	12.8	...
34	-5.74	1.30	8.74	-8.193	0.002	14.598	0.007	18.7	55.1	36
35*	-5.51	0.65	8.24	-8.555	0.022	14.083	0.071	1.8	4.8	...
36	-4.62	1.74	9.12	-16.734	0.004	8.241	0.011	6.2	33.0	37
37	-4.30	1.74	8.76	-7.981	0.010	14.622	0.009	12.4	69.8	38
38	-4.08	1.52	9.47	-7.822	0.014	-3.618	0.048	2.1	11.2	...
39*	-3.72	0.65	9.58	-17.347	0.037	4.073	0.048	2.8	7.5	39
40*	-3.30	0.65	10.93	-13.892	0.019	15.022	0.059	1.2	3.0	...
41	-3.16	2.61	9.03	-7.811	0.009	14.892	0.019	9.4	62.0	41
42	-3.09	2.39	9.26	-16.914	0.011	8.125	0.023	3.9	26.3	42
43	-3.05	2.17	8.75	-16.624	0.011	4.791	0.021	9.0	60.1	40
44*	-2.67	0.65	8.33	-7.722	0.033	14.190	0.027	1.2	2.9	...
45	-2.40	2.61	9.14	-16.370	0.008	9.381	0.023	13.2	95.3	45
46*	-2.40	0.87	11.11	-14.067	0.013	15.123	0.049	1.4	3.6	44
47*	-2.36	1.09	8.42	-16.199	0.033	4.248	0.097	4.6	14.1	43
48	-1.83	1.96	8.08	-15.931	0.013	4.670	0.034	5.2	38.6	46
49*	-1.61	0.65	8.63	-16.528	0.012	5.067	0.036	2.2	6.0	...
50*	-1.16	0.65	8.27	-16.157	0.011	5.014	0.022	2.0	5.1	47
51	-0.54	1.30	8.48	-15.780	0.019	9.080	0.040	1.7	12.6	...
52	-0.47	1.74	9.27	-11.556	0.008	-2.679	0.026	3.0	18.7	50
53	-0.33	0.87	9.83	1.767	0.033	7.487	0.068	2.2	6.2	51
54*	0.39	0.65	7.12	-14.744	0.034	3.762	0.065	1.8	4.1	52
55	1.49	1.30	8.52	-10.627	0.009	-2.226	0.030	3.6	14.6	56
56	1.49	1.30	10.65	1.969	0.011	1.927	0.019	2.7	12.1	55
57	1.55	1.96	8.71	-11.052	0.013	-2.276	0.033	3.4	24.7	53
58	1.58	1.30	8.10	-11.766	0.013	12.997	0.035	3.7	13.7	57
59*	1.70	0.65	9.30	-1.642	0.023	12.725	0.052	1.3	3.1	...
60	1.85	0.87	8.33	-12.225	0.033	13.001	0.036	5.3	9.5	...
61	2.30	1.95	7.55	-11.316	0.010	12.614	0.023	8.0	52.1	58
62	2.85	1.74	8.01	-12.161	0.008	12.666	0.029	2.5	13.7	...
63	3.07	1.09	8.78	0.646	0.006	3.962	0.020	2.3	8.7	...
64	3.19	1.74	7.03	-11.131	0.017	12.125	0.029	10.8	34.3	61
65	3.35	1.30	7.68	-2.163	0.020	0.787	0.047	1.3	6.8	60

Table 2—Continued

ID	V_{LSR} (km s^{-1})	Δu	r (mas)	x (mas)	σ_x	y (mas)	σ_y	P (Jy)	S (Jy km s^{-1})	Match ID Epoch 2 (11)
(1)	(2)	(3)	(4)	(5)	(6)	(7)	(8)	(9)	(10)	(11)
66	3.50	1.52	6.85	-10.396	0.011	12.258	0.025	5.1	23.6	62
67	4.13	1.95	7.66	-12.283	0.017	12.167	0.028	2.9	12.7	...
68	4.17	0.87	7.46	-10.183	0.011	-1.255	0.053	1.7	5.5	64
69	4.27	1.09	7.42	-3.501	0.016	-0.097	0.053	1.4	5.1	...
70	4.29	1.74	8.55	0.434	0.010	4.042	0.026	2.5	14.7	66
71	4.78	1.52	7.37	-12.552	0.013	11.604	0.020	8.0	35.3	67
72	5.04	1.74	6.40	-1.921	0.007	8.073	0.026	2.5	13.7	...
73*	5.44	0.87	6.93	-3.062	0.011	0.916	0.038	1.2	3.6	...
74	5.56	1.30	5.79	-13.234	0.012	3.534	0.023	2.9	12.2	72
75	5.67	1.52	5.94	-10.333	0.004	11.302	0.014	5.5	22.0	70
76*	5.72	0.87	6.84	-4.629	0.011	-0.132	0.038	1.5	5.7	71
77	6.06	0.87	7.13	-3.665	0.008	0.137	0.026	1.7	5.4	...
78	7.05	1.74	6.46	-8.987	0.013	-0.517	0.027	5.3	25.7	74
79	7.23	1.30	6.08	-7.467	0.014	11.923	0.042	1.4	6.3	73
80	7.51	1.09	7.87	-0.253	0.016	4.125	0.048	1.9	6.6	...
81	7.91	1.74	6.48	-9.070	0.010	-0.522	0.033	4.7	26.1	...
82	7.92	2.39	5.13	-12.679	0.008	3.906	0.022	2.8	19.6	76
83	8.09	2.39	6.21	-8.201	0.013	12.065	0.036	3.7	25.2	78
84	9.15	1.96	5.89	-8.943	0.006	0.052	0.020	5.1	31.3	80
85	9.31	1.30	5.73	-8.309	0.008	11.587	0.017	3.5	16.1	81
86	12.98	1.09	2.41	-5.522	0.008	5.632	0.026	2.9	10.8	82
87	12.99	1.09	4.44	-6.258	0.007	9.977	0.029	1.8	6.4	...

Note. — The representations of columns (1)-(11) are the same as in Table 1.

*Feature which can not be well represented by a Gaussian curve.

^RReference feature.

Table 3. Sources with the detected contraction of SiO maser shell.

Source	stellar phase ϕ	Contraction velocity km s^{-1}	Reference
R Aqr	0.78 – 1.04	4.2 ± 0.9	Boboltz et al. (1997)
TX Cam	0.50 – 0.65	5 – 10	Diamond & Kemball (2003)
VX Sgr	0.75 – 0.80	4.1 ± 0.6	Chen et al. (2006)
AH Sco	~ 0.55	12.7 ± 0.7	this work

Table 4. Best-fit model for the SiO maser kinematics in AH Sco.

v_{0x} (km s^{-1})	v_{0y} (km s^{-1})	v_{0z} (km s^{-1})	V_1 (km s^{-1})	α	d (kpc)	Reduced χ^2
3.8 ± 0.3	-0.9 ± 0.4	-5.2 ± 0.4	-14.1 ± 1.4	-0.54 ± 0.16	2.26 ± 0.19	3.58

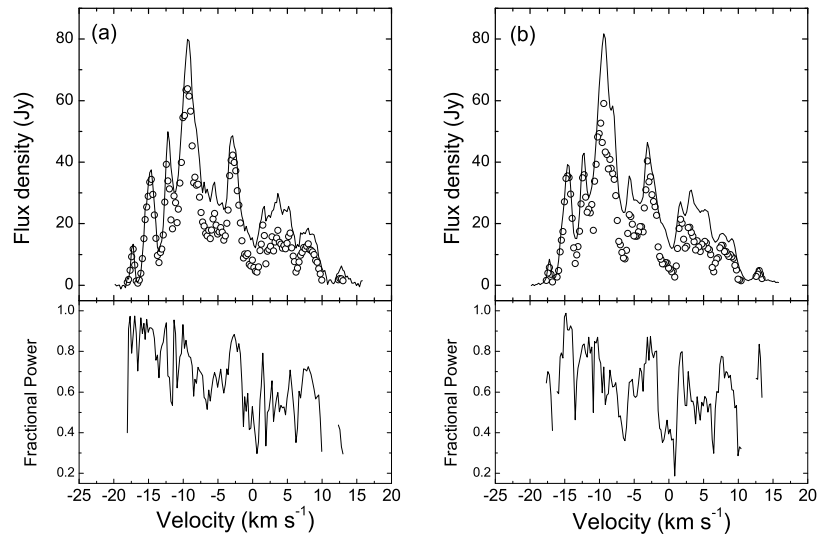


Fig. 1.— Top: Comparison of total power (solid line) to cross power (open circle) of 43 GHz $v=1$, $J=1-0$ SiO maser emission toward AH Sco obtained on (a) March 8, 2004 and (b) March 20, 2004. Bottom: The corresponding fraction power (cross/total) detected by the high-resolution VLBA observations.

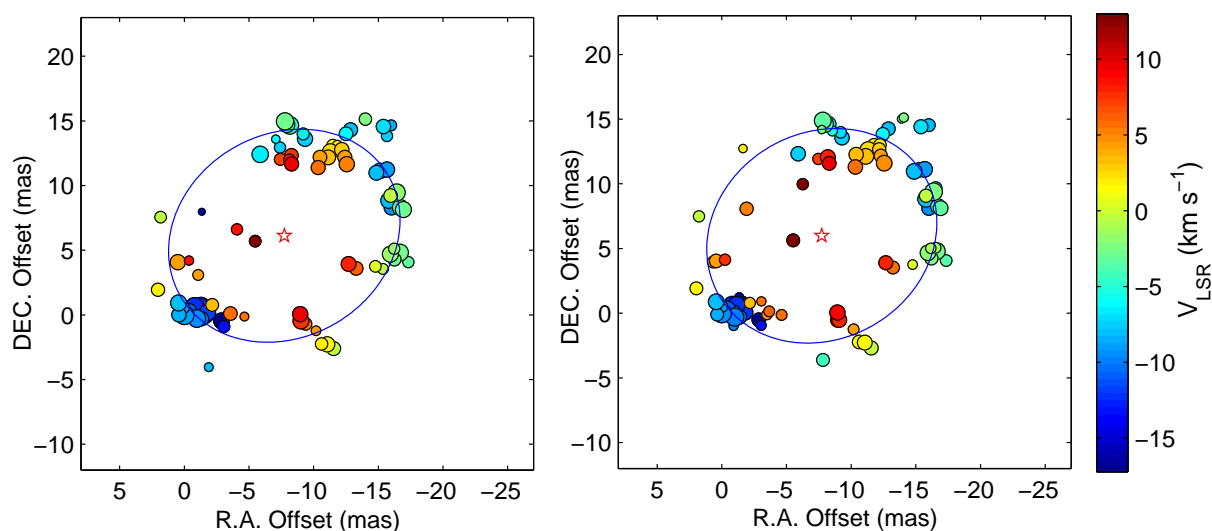


Fig. 2.— VLBI images of 43 GHz $v=1$, $J=1-0$ SiO maser emission toward AH Sco obtained on (a) March 8, 2004 and (b) March 20, 2004. Each maser feature is represented by a filled circle whose area is proportional to the logarithm of the flux density, and the color indicates its Doppler velocity with respect to the local standard of rest. Its stellar velocity is about -7 km s^{-1} . Errors in the positions of the features are smaller than the data points. The ellipse indicates the least-squares fit to the maser distribution for each epoch. The fitted center of ellipse model is marked by the red star.

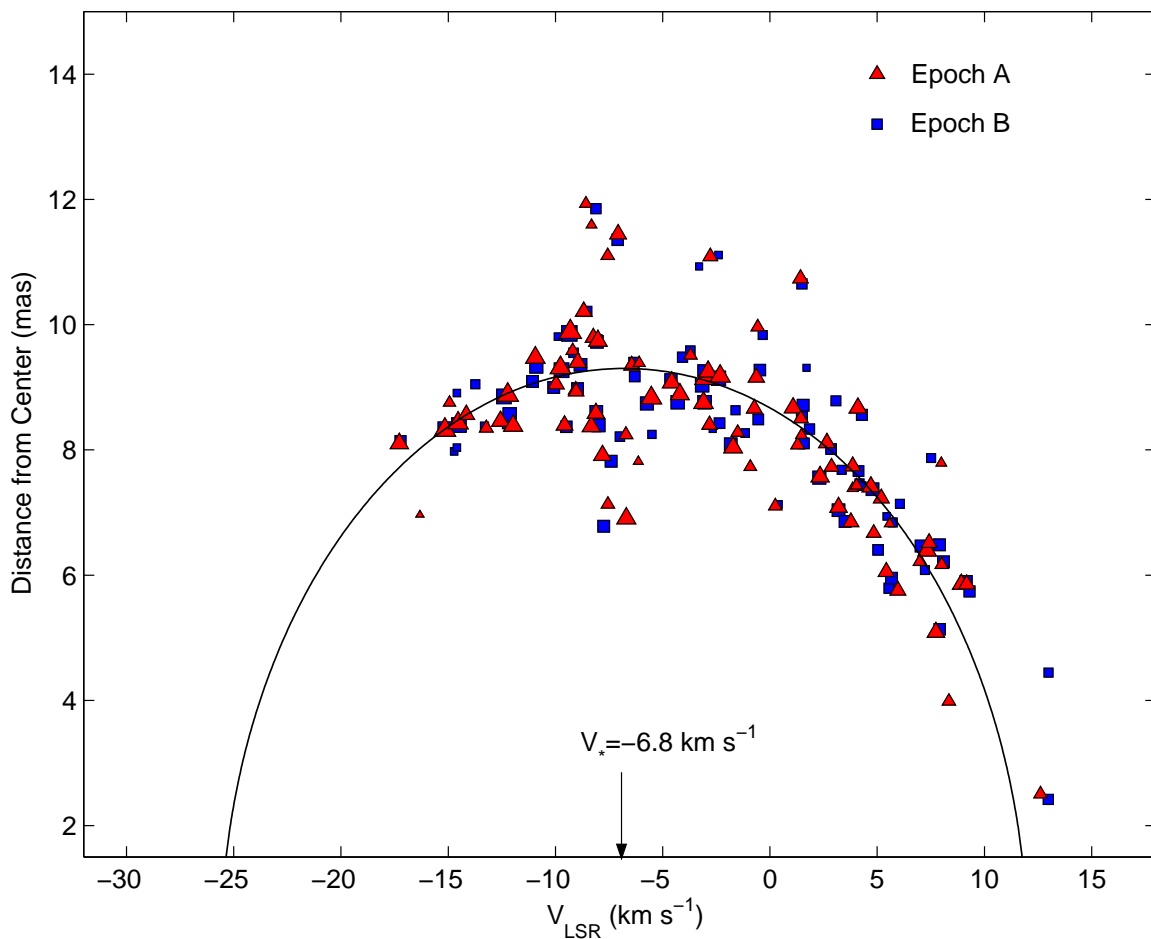


Fig. 3.— Distance of maser features from the fitted position of central star (in Fig. 2) versus their LOS velocity for epochs A and B. Maser features of the different epochs are denoted by different color symbols whose area is proportional to the logarithm of the flux density. The plot suggests that the higher-velocity maser features lie closer to the central star, which can be well explained by the uniformly expanding thin shell model. Indicated by the downward arrow is the systemic velocity of AH Sco of -6.8 km s^{-1} , obtained from the best-fitting thin-shell model (shown by the curve).

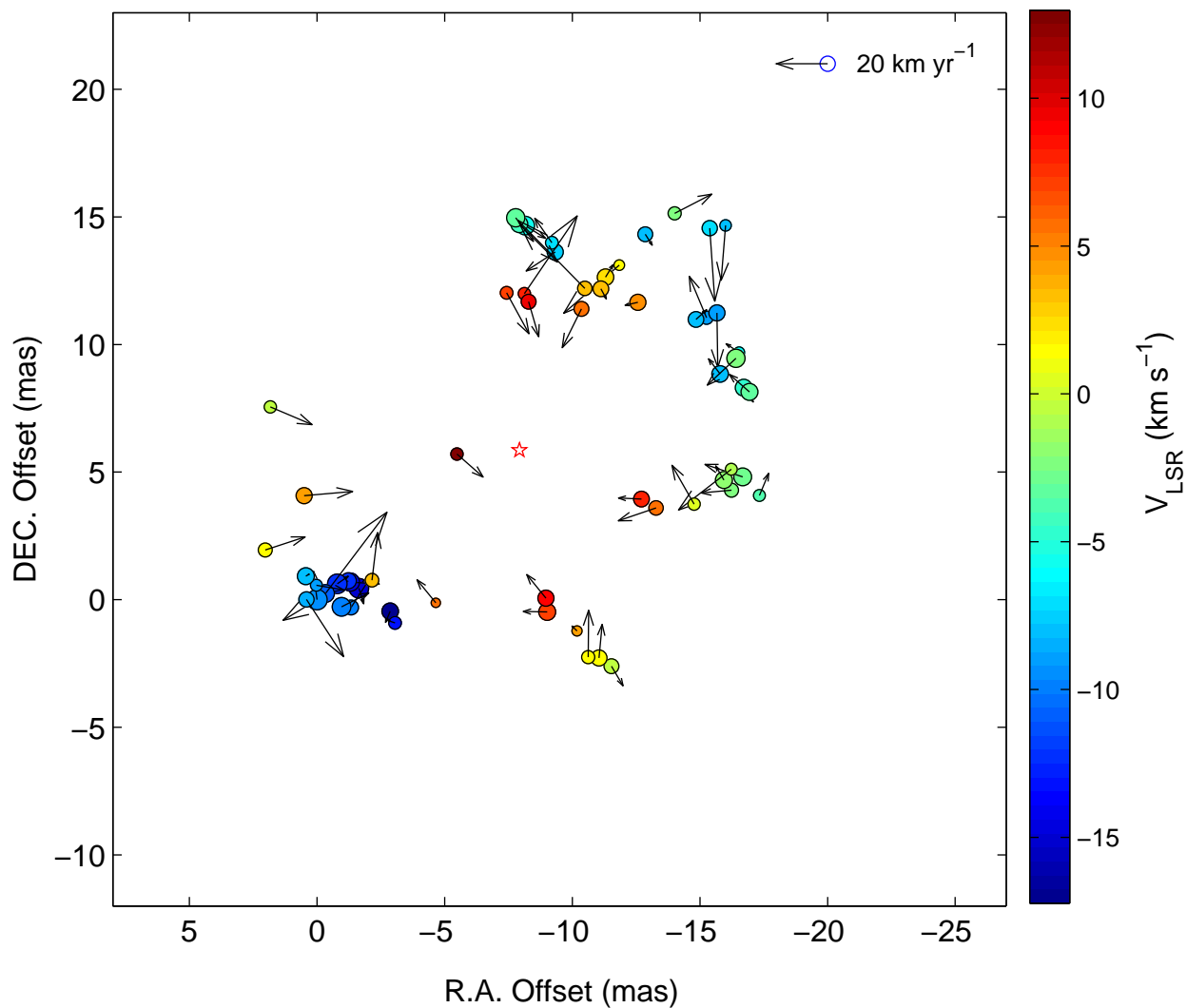


Fig. 4.— Distribution of proper motion velocity vectors of the matched maser features at an assumed distance of 2.26 kpc. The length of the vector is proportional to the velocity. The mean proper motion vector has been subtracted from each of the determined proper motion vectors. The color and size of symbols are the same as that shown in Fig. 2. Red star represents the fitted center of ellipse model to maser distribution (see Sect. 3.1).